Available online at www.sciencedirect.com
ScienceDirect
Journal of Computational Physics 226 (2007) 477–493
JOURNAL OF COMPUTATIONAL PHYSICS
www.elsevier.com/locate/jcp

Domain decomposition method for Maxwell's equations: Scattering off periodic structures

Achim Schädle [a,*,1], Lin Zschiedrich [a,b], Sven Burger [a,b], Roland Klose [a,1], Frank Schmidt [a,b]

[a] *Zuse Institute Berlin, Numerical Analysis and Modelling, Takustrasse 7, D-14195 Berlin, Germany*
[b] *JCMwave GmbH, Haarer Str. 14a, D-85640 Putzbrunn, Germany*

Received 14 February 2006; received in revised form 29 January 2007; accepted 19 April 2007
Available online 1 May 2007

Abstract

We present a domain decomposition approach for the computation of the electromagnetic field within periodic structures. We use a Schwarz method with transparent boundary conditions at the interfaces of the domains. Transparent boundary conditions are approximated by the perfectly matched layer method (PML). An adaptive strategy to determine optimal PML parameters is developed. Thus we can treat Wood anomalies appearing in periodic structures.

We focus on the application to typical EUV lithography line masks. Light propagation within the multilayer stack of the EUV mask is treated analytically. This results in a drastic reduction of the computational costs and allows for the simulation of next generation lithography masks on a standard personal computer.

MSC: 65N55

Keywords: Domain decomposition; Conical diffraction; Electro-magnetic scattering; Maxwell's equations; Lithography; EUV; Finite elements; Perfectly matched layer method

1. Introduction

The fabrication of semiconductor chips is based on an optical projection system, which transfers the pattern from the photolithography mask onto the chip. State of the art photolithography tools are operated with light of a vacuum wavelength $\lambda \sim 193$ nm [5]. Currently tools are developed that employ extreme ultraviolet light (EUV) with a vacuum wavelength $\lambda \sim 13$ nm. At this wavelength there are no materials available that are transparent, hence mask and lenses have to be replaced by mirrors, which are formed of multilayer stacks.

* Corresponding author.
E-mail addresses: schaedle@zib.de (A. Schädle), lin.zschiedrich@jcmwave.com (L. Zschiedrich), sven.burger@jcmwave.com (S. Burger), klose@zib.de (Roland Klose), frank.schmidt@zib.de (F. Schmidt).
[1] Supported by the DFG Research Center MATHEON "Mathematics for key technologies" in Berlin.

0021-9991/$ - see front matter © 2007 Elsevier Inc. All rights reserved.
doi:10.1016/j.jcp.2007.04.017

A typical section of an EUV lithography line mask is depicted in Fig. 1. The light is incident from above and is reflected back. The line on the mask absorbs some light, thus casting a shadow.

The line mask is invariant in x_3 direction and periodic with period a in x_1 direction. The multilayer stack may consist of more than 100 layers; the thickness of each layer is about a quarter of a wavelength. The incident wave is twofold oblique – oblique with respect to the mask plane and oblique with respect to the multilayer structure. The polarization of the incident field is arbitrary.

In Section 2 we introduce the mathematical setting of the arising scattering problem and derive the radiating boundary condition in terms of Fourier modes. Further, we show that the exterior Dirichlet as well as Neumann boundary value problem is ill-posed in the presence of so called *Wood anomalies* [19].

To deal with the large computational domains we propose a domain decomposition method, described in Section 5. The multilayer sub-domain is treated semi-analytically, c.f. Section 2.4, whereas the other sub-domains are discretized by the finite element method using the PML method to approximate transparent boundary conditions. The PML method goes back to Bérenger [2]; convergence of the method was proven in [16,17] and [15] for non-periodic problems. As is shown in Section 3 the PML method fails for periodic domains in the presence of Wood anomalies. As a remedy we propose in Section 3.2 a new automatic adaption of the layer size and the spatial discretization within the PML. This leads to quasi infinitely thick layers in the presence of Wood anomalies. In Section 4 a variational formulation is used to couple the PML to the interior problem.

In contrast to Elschner et al. [12,11] the electromagnetic field $\mathbf{E} = (E_1, E_2, E_3)$ is discretized with higher order Whitney elements for the (E_1, E_2) component and Lagrange elements of the same order in the E_3 component. This allows for the accurate evaluation of Fourier coefficients needed for the coupling to the multilayer stack.

The Schwarz algorithm proposed in Section 5 uses transparent boundary conditions at the interfaces. For the scalar Helmholtz equation Després and Shaidurov proposed to balance the energy fluxes across domain interfaces [10,27]. This idea of balancing the energy flux was further examined in [1,6,7,9,14]. One may view this transmission condition as a first order transparent boundary condition. The Schwarz algorithm for Helmholtz scattering problems with transparent boundary conditions at the domain interfaces is considered in [23,28]. In [13] the objective in the construction of local transmission conditions is not to balance the energy flux, but to optimize the transmission condition to speed up convergence. Local optimized transmission conditions for the time-harmonic Maxwell's equations are considered in [18,22].

The idea of using transparent boundary conditions as transmission conditions is motivated as follows. Suppose there are two obstacles A and B and an incident wave. One could then calculate the scattered field of each of the obstacles separately. The scattered field of obstacle A is then added to the incoming field for B, and vice versa. Iterating this procedure the scattered field is corrected in each step. In each sub-domain only a simplified scattering problem is solved.

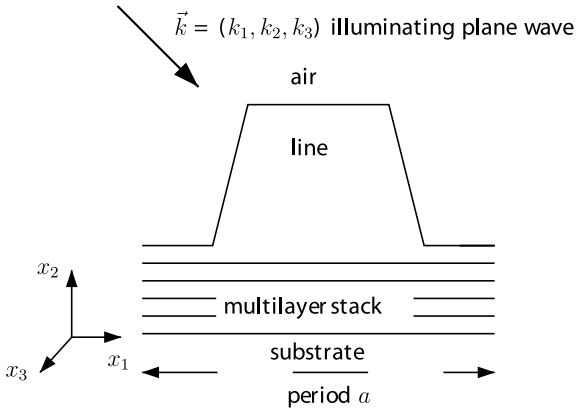

Fig. 1. Layout of an EUV lithography line mask. The structure is periodically repeated in x_1 direction and invariant in x_3 direction. The illuminating light is a plane wave with an arbitrary wave vector $\vec{k} = (k_1, k_2, k_3)$.

2. Scattering off periodic line masks

Scattering off a periodic line mask is described by a Maxwell scattering problem, with Bloch-periodic boundary condition in x_1 direction and transparent boundary conditions in x_2 direction. The dependency on the x_3 component is eliminated.

2.1. Maxwell's equation

We consider electromagnetic scattering problems governed by the time-harmonic Maxwell's equations

$$\mathbf{curl}\,\mu^{-1}(\vec{x})\mathbf{curl}\,\mathbf{E}(\vec{x}) - \omega^2\varepsilon(\vec{x})\mathbf{E}(\vec{x}) = 0, \tag{1a}$$

$$\mathbf{div}\,\varepsilon(\vec{x})\mathbf{E}(\vec{x}) = 0, \tag{1b}$$

with angular frequency ω. The dielectric tensor ε and the permeability tensor μ are L^∞. Additionally we assume, that the tensors ε and μ do not depend on x_3, that they are periodic functions in x_1 with period a, i.e. $\varepsilon(\vec{x}+(a,0,0)) = \varepsilon(\vec{x})$, $\mu(\vec{x}+(a,0,0)) = \mu(\vec{x})$, and that they are constant for $x_2 > x_{2,+}$ and $x_2 < x_{2,-}$ with $x_{2,+} > x_{2,-}$. For simplicity the dielectric and the permeability tensors are assumed to be isotropic.

A scattering problem may be defined as follows: Given an incoming electric field $\mathbf{E}_{\text{inc}}$ satisfying the time-harmonic Maxwell's equation (1a) for $x_2 > x_{2,+}$ and $x_2 < x_{2,-}$, compute the total electric field $\mathbf{E}$, which satisfies (1a) in $\mathbb{R}^3$, such that the scattered field $\mathbf{E}_{\text{sc}} = \mathbf{E} - \mathbf{E}_{\text{inc}}$ defined for $x_2 > x_{2,+}$ and $x_2 < x_{2,-}$ meets the radiation condition given in Section 2.2.

It is possible to restrict the problem onto a two dimensional strip $[0,a]\times\mathbb{R}$ provided that the incoming field is Bloch periodic in x_1 [4] and depends harmonically on x_3, i.e. $\mathbf{E}_{\text{inc}}(x_1+a,x_2,x_3) = \widetilde{\mathbf{E}}_{\text{inc}}(x_1,x_2)\mathrm{e}^{\mathrm{i}k_1 a}\mathrm{e}^{\mathrm{i}k_3 x_3}$, where $\widetilde{\mathbf{E}}_{\text{inc}}$ is a periodic function in x_1 with period a. The important case of an incoming plane wave meets these restrictions. The total field $\mathbf{E}$ as well as the scattered field are then themselves Bloch periodic in x_1 and depend harmonically on x_3.

In what follows $\mathbf{E}$, $\mathbf{E}_{\text{inc}}$ and $\mathbf{E}_{\text{sc}}$ denote the restriction of the respective field onto the strip $[0,a]\times\mathbb{R}$. This strip is split into domains $\Omega = [0,a]\times[x_{2,-},x_{2,+}]$, $\Omega_+ = [0,a]\times[x_{2,+},\infty]$ and accordingly Ω_-. With the definitions

$$\mathbf{curl}_3\mathbf{E} = (\partial_{x_2}E_3 - \mathrm{i}k_3E_2, \mathrm{i}k_3E_1 - \partial_{x_1}E_3, \partial_{x_1}E_2 - \partial_{x_2}E_1)^{\mathrm{T}},$$

$$\mathbf{div}_3\varepsilon\mathbf{E} = \partial_{x_1}\varepsilon E_1 + \partial_{x_2}\varepsilon E_2 + \mathrm{i}k_3\varepsilon E_3$$

the scattering problem splits into an interior domain problem

$$\begin{aligned} &\mathbf{curl}_3\mu^{-1}\mathbf{curl}_3\mathbf{E}(x_1,x_2) - \omega^2\varepsilon\mathbf{E}(x_1,x_2) = 0 \quad (x_1,x_2)\in\Omega,\\ &\mathbf{E}(0,x_2) - \mathbf{E}(a,x_2)\mathrm{e}^{\mathrm{i}k_1 a} = 0, \end{aligned} \tag{2}$$

an upper exterior domain problem

$$\begin{aligned} &\mathbf{curl}_3\mu_+^{-1}\mathbf{curl}_3\mathbf{E}_{\text{sc},+}(x_1,x_2) - \omega^2\varepsilon_+\mathbf{E}_{\text{sc},+}(x_1,x_2) = 0 \quad (x_1,x_2)\in\Omega_+,\\ &\mathbf{E}_{\text{sc},+}(0,x_2) - \mathbf{E}_{\text{sc},+}(a,x_2)\mathrm{e}^{\mathrm{i}k_1 a} = 0 \end{aligned} \tag{3}$$

and a lower exterior problem on Ω_- of similar type.

Subproblems (2) and (3) are coupled by the following matching conditions on the boundary $x_2 = x_{2,+}$:

$$(\mathbf{E} - (\mathbf{E}_{\text{sc},+} + \mathbf{E}_{\text{inc},+}))\times\vec{n}_+ = 0, \tag{4a}$$

$$(\mu^{-1}\mathbf{curl}_3\,\mathbf{E} - (\mu_+^{-1}\mathbf{curl}_3\,\mathbf{E}_{\text{sc},+} + \mu_+^{-1}\mathbf{curl}_3\,\mathbf{E}_{\text{inc},+}))\times\vec{n}_+ = 0, \tag{4b}$$

where $\vec{n}_+ = (0,-1,0)^{\mathrm{T}}$ denotes the unit normal vector. An analogous condition holds on the boundary $x_2 = x_{2,-}$, coupling the interior and the lower exterior problem.

2.2. Radiation condition for homogeneous exterior domain problem

The exterior domain problem lacks a radiation condition. As both upper and lower exterior problems can be treated similarly, we consider the upper exterior domain problem only and drop the "+". Without loss of generality and to simplify matters, we assume that $x_{2,+} = 0$.

Due to the periodicity of $\mathbf{E}_{\mathrm{sc}} \exp(-\mathrm{i}k_1 x_1)$ the field has an expansion into Fourier modes

$$\mathbf{E}_{\mathrm{sc}}(x_1, x_2) = \mathrm{e}^{+\mathrm{i}k_1 x_1} \sum_{n\in\mathbb{Z}} \vec{e}_n(x_2) \mathrm{e}^{\mathrm{i}x_1 n 2\pi/a}, \tag{5}$$

with the Fourier coefficients

$$\vec{e}_n(x_2) = \frac{1}{a} \int_0^a \mathrm{e}^{-\mathrm{i}k_1\xi} \mathbf{E}_{\mathrm{sc}}(\xi, x_2) \mathrm{e}^{-\mathrm{i}\xi(n2\pi/a)} \,\mathrm{d}\xi.$$

The field $\mathbf{E}_n(x_1, x_2, x_3) = \vec{e}_n(x_2) \exp(\mathrm{i}(n2\pi/a + k_1)x_1) \exp(\mathrm{i}k_3 x_3)$ is a solution of Maxwell's equation (1a) for $x_2 > 0$. Hence inserting $\mathbf{E}_n$ in (1a) yields

$$\mathbf{E}_n(x_1, x_2, x_3) = \vec{e}_{n,+} \mathrm{e}^{\mathrm{i}(n2\pi/a+k_1)x_1} \mathrm{e}^{\mathrm{i}k_{2,n}x_2} \mathrm{e}^{\mathrm{i}k_3 x_3} + \vec{e}_{n,-} \mathrm{e}^{\mathrm{i}(n2\pi/a+k_1)x_1} \mathrm{e}^{-\mathrm{i}k_{2,n}x_2} \mathrm{e}^{\mathrm{i}k_3 x_3},$$

with $k_{2,n} = \sqrt{k_0^2 - (n2\pi/a + k_1)^2 - k_3^2}$, where the branch cut of the square root is along the negative real axis and $k_0 = \omega\sqrt{\mu\varepsilon}$. From this representation it is easily seen that the field can be decomposed into an incoming and an outgoing part.

We have to distinguish three cases:

(1) $\mathrm{Re}\, k_{2,n} > 0$, $\mathrm{Im}\, k_{2,n} = 0$ (*propagating mode*) Both parts are propagating plane waves. The second part transports energy in the $-x_2$ direction. We therefore require $\vec{e}_{n,-} = 0$. This corresponds to the well known Sommerfeld radiation condition.
(2) $\mathrm{Re}\, k_{2,n} = 0$, $\mathrm{Im}\, k_{2,n} > 0$ (evanescent mode) The first part is evanescent in x_2 direction while the second part increases exponentially. Therefore we again require $\vec{e}_{n,-} = 0$.
(3) $k_{2,n} = 0$ (anomalous mode) In this case both parts are equal and constant in x_2 direction. Energy is only transported in x_1 and x_3 directions. For the sake of a consistent notation we set $\vec{e}_{n,-} = 0$.

Hence the correct radiation boundary condition is $\vec{e}_{n,-} = 0$ for all $n \in \mathbb{Z}$, such that the Fourier coefficients of the scattered field are given by $\vec{e}_{n,\mathrm{sc}} = \vec{e}_{n,+}$. The anomalous case is rare. For example for $k_1 = 0$ and $k_3 = 0$ it only occurs if $a = 2\pi/(k_0 n)$.

2.3. Ill-posed exterior Dirichlet/Neumann boundary value problems

In our previous paper [23] the DtN operator was used to state the coupling between the different domains. However the DtN operator may not exist in the periodic setting – the exterior Dirichlet problem is ill-posed in the presence of anomalous modes.

This may be seen by rewriting Maxwell's equations separated in Fourier modes. With $\vec{k}_n = (k_1 + n2\pi/a, k_{2,n}, k_3)$ the vectors $\vec{e}_{n,\mathrm{sc}}$ satisfy the algebraic relations

$$-\vec{k}_n \times (\vec{k}_n \times \vec{e}_{n,\mathrm{sc}}) - k_0^2 \vec{e}_{n,\mathrm{sc}} = 0, \tag{6a}$$

$$\vec{e}_{n,\mathrm{sc}} \cdot \vec{k}_n = 0. \tag{6b}$$

The first relation stems from Eq. (1a) and the second relation from Eq. (1b). If $j \in \mathbb{Z}$ corresponds to an anomalous mode, that is $\vec{k}_j = (k_1 + j2\pi/a, 0, k_3)$, then $\vec{e}_{j,\mathrm{sc}} = (0, 1, 0)$ satisfies (6). Hence $\mathbf{E}_{sc} = \vec{e}_{n,\mathrm{sc}} \exp(\mathrm{i}\vec{k}_j \cdot \vec{x})$ is a solution of the exterior domain problem with zero Dirichlet tangential boundary values. Therefore the Dirichlet boundary value problem is not uniquely solvable. Furthermore due to the divergence condition (6b) the vector $\vec{e}_{j,\mathrm{sc}}$ must be perpendicular to $\vec{k}_j$. Hence for boundary values with $(d_1, 0, d_3) \cdot \vec{k}_j \neq 0$ the problem is not solvable at all.

By an analogous argument one shows that the Neumann boundary value problem is also ill-posed in the presence of anomalous modes.

What is worse, there may exist guided waves,[2] and hence the problem is ill-posed; and this ill-posedness is not related to the radiation condition. Assume $\mu = \mu_0$ and $\varepsilon(x) = \varepsilon_0$ for $|x_2| > L$ and $\varepsilon(x) = \varepsilon_1$ else; pick k_1, k_3 such that

$$\omega^2\varepsilon_0\mu_0 < k_1^2 + k_3^2 < \omega^2\varepsilon_1\mu_0;$$

define

$$k_2 = \sqrt{\omega^2\varepsilon_1\mu_0 - (k_1^2 + k_3^2)}, \quad \xi_2 = \sqrt{(k_1^2 + k_3^2) - \omega^2\varepsilon_0\mu_0}$$

and

$$\mathbf{E}(x_1, x_2, x_3) = \widetilde{E}(x_1, x_2)\mathrm{e}^{\mathrm{i}k_3x_3}, \quad \widetilde{E}(x_1, x_2) = \mathrm{e}^{\mathrm{i}k_1x_1}e_3(x_2)\hat{x}_3,$$

with

$$e_3(x_2) = \begin{cases} \cos(k_2x_2)/\cos(k_2L) & \text{for } |x_2| \leqslant L, \\ \mathrm{e}^{-\xi_2(|x_2|-L|)} & \text{for } |x_2| > L. \end{cases}$$

Assume that the width of the layer L is such that

$$k_2\tan(k_2L) = \xi_2.$$

This implies that both e_3 and $\partial_{x_2}e_3$ are continuous at the interfaces $x_2 = \pm L$. Then $\widetilde{E}(x_1, x_2) \in H(\mathbf{curl}_3)$ doesn't vanish, is Bloch periodic and satisfies the k_3-Maxwell equation with no source term and with the good behavior at infinity. Thus the problem is ill-posed.

In practice however some of EUV line mask materials are dissipative (their permittivity has an imaginary part) and guided waves do not exist in this case.

2.4. Scattering off an isotropic multilayer stack – the Transfer Matrix method

The Transfer Matrix method which according to [20] was developed by Schuster [26], will be reviewed here shortly. For more details, the reader is referred to [20,3].

Suppose we are in the situation of Fig. 1. Let us consider only the material stack with m finite layers positioned at $x_{2,j}$, $j = 0, \ldots, m$, with $x_{2,j} < x_{2,j+1}$. For $j = 1, \ldots, m$ the layer stack is given by the layer thicknesses $x_{2,j} - x_{2,j-1}$ and the material coefficients ε_j and μ_j. Additionally for the semi-infinite half-spaces we have ε_0, μ_0 and ε_{m+1}, μ_{m+1}. Since the Transfer Matrix algorithm is applied to each Fourier mode $k_{1,n}$ separately, we drop the sub-index n in this section. In each layer local wave vectors $\vec{k}_j = (k_1, k_{2,j}, k_3)$ and $\overleftarrow{k} = (k_1, -k_{2,j}, k_3)$ with $k_{2,j} = \sqrt{\omega^2\epsilon_j\mu_j - k_1^2 - k_3^2}$ are defined, such that $\mathrm{Re}\,k_{2,j} \geqslant 0$ and $\mathrm{Im}\,k_{2,j} \geqslant 0$. For a given excitation $\mathbf{E}_{\mathrm{inc}} = A_{m+1,\mathrm{inc}}\exp(\mathrm{i}\vec{k}_{m+1}\vec{x}) + B_{m+1,\mathrm{inc}}\exp(\mathrm{i}\overleftarrow{k}_{m+1}\vec{x})$ we want to calculate the reflected field $\mathbf{E}_{\mathrm{sc}} = A_{m+1,sc}\exp(\mathrm{i}\vec{k}_{m+1}\vec{x})$. From Snell's law we obtain that the field in each layer is given by $\mathbf{E}_j = A_j\exp(\mathrm{i}\vec{k}_j\vec{x}) + B_j\exp(\mathrm{i}\overleftarrow{k}_j\vec{x})$. In the lower semi-infinite half space a purely outgoing field is assumed, i.e. $A_0 = 0$. In the layers we have 6 m unknowns – each A or B has 3 components. In the lower semi-infinite domain the only unknowns are the three components of B_0 of the purely outgoing field. In the upper semi-infinite domain there are six unknowns for the excitation and three for the reflected field.

These unknowns are determined by the following linear conditions arising from Maxwell's equations: there are $1 + 2 + 2m + 1$ equations from the divergence condition. At the $m + 1$ boundaries of the layers there are $2(m + 1)$ matching conditions for the tangential components of the Dirichlet data and the same number of conditions from matching the Neumann data.

$$\left.\begin{array}{l} \mathbf{E}_{j-1} \times \vec{n} = \mathbf{E}_j \times \vec{n} \\ \mu_{j-1}\mathbf{curl}\,\mathbf{E}_{j-1} \times \vec{n} = \mu_j\mathbf{curl}\,\mathbf{E}_j \times \vec{n} \end{array}\right\} \text{ at } \vec{x} = \vec{x}_{j-1} \quad \text{for } j = 1, \ldots, n+1.$$

Here $\mathbf{E}_0 := \mathbf{E}_{\mathrm{inc}} + \mathbf{E}_{\mathrm{sc}}$. The missing four conditions are the tangential components of the Dirichlet and Neumann data of the given incoming field.

[2] This was pointed out by one of the referees of the paper. And we are happy to include her/his consideration here.

These yield a linear system of equations. To avoid large condition numbers due to the complex material tensors, in each layer ansatz functions with amplitude equal to +1 at the layer midpoint are used.

3. Perfectly matched layer method

In the previous section we discussed the homogenous exterior domain problem and derived transparent boundary conditions for each Fourier mode. Transforming back from Fourier space, this boundary condition would be non-local and somehow the anomalous case had to be treated separately. The perfectly matched layer method is an approximate transparent boundary condition, introducing only small reflections that are well under control. A major advantage of the PML method is, that it fits in the finite-element framework, described shortly in Section 4.2, and thus does not introduce "full" blocks in the discretization. The derivation of the PML closely follows [8]. Opposed to a more standard PML method we fix the damping factor σ, but chose the thickness and the discretization of the layer adaptively.

3.1. General presentation

The PML method is based on a complex continuation of the scattered field. For $\gamma = (1 + \mathrm{i}\sigma)$, $0 < \sigma \in \mathbb{R}$, we define the complex continued field

$$\mathbf{E}_\gamma = \sum_{n\in\mathbb{Z}} \vec{e}_{\mathrm{sc},n} \mathrm{e}^{\mathrm{i}(n2\pi a + k_1)x_1} \mathrm{e}^{\mathrm{i}k_{n,2}\gamma x_2} \mathrm{e}^{\mathrm{i}k_3 x_3}. \tag{7}$$

With the definition

$$\mathbf{curl}_{3,\gamma}\,\mathbf{E}_\gamma = \left(\frac{1}{\gamma}\partial_{x_2}E_{\gamma,3} - \mathrm{i}k_3E_{\gamma,2}, \mathrm{i}k_3E_{\gamma,1} - \partial_{x_1}E_{\gamma,3}, \partial_{x_1}E_{\gamma,2} - \frac{1}{\gamma}\partial_{x_2}E_{\gamma,1}\right)$$

the field $\mathbf{E}_\gamma$ satisfies Maxwell's equations (3) with $\mathbf{curl}_3$ replaced by $\mathbf{curl}_{3,\gamma}$. In the absence of anomalous modes $\mathbf{E}^\gamma$ is evanescent for $x_2 \to \infty$

$$|\mathbf{E}_\gamma| \leqslant \mathrm{e}^{-\kappa x_2} C,$$

with $\kappa = \min_{n\in\mathbb{Z}}\{\mathrm{Im}\,k_{n,2}, \sigma\mathrm{Re}\,k_{n,2}\}$. The idea is to restrict the complex continued exterior domain problem to a truncated domain $\Omega_\rho = [0,a]\times[0,\rho]$ and to impose a zero Dirichlet boundary condition at $x_2 = \rho$. In case κ is small or even +0, i.e. if we are "close" to an anomalous mode a special adaptive PML is used, where the thickness ρ is increased like $1/\kappa$ and the discretization points are distributed with an exponentially increasing mesh width guaranteeing an effective discretization, c.f. Section 3.2. Thus the unbounded exterior problem (3) is replaced by the truncated exterior domain problem

$$\begin{aligned}
&\mathbf{curl}_3\,\mu_+^{-1}\mathbf{curl}_3\,\mathbf{E}_{\gamma,\rho}(x_1,x_2) - \omega^2\varepsilon_+\mathbf{E}_{\gamma,\rho}(x_1,x_2) = 0 \quad (x_1,x_2)\in\Omega_\rho,\\
&\mathbf{E}_{\gamma,\rho}(0,x_2) - \mathbf{E}_{\gamma,\rho}(a,x_2)\mathrm{e}^{\mathrm{i}k_1 a} = 0,\\
&\mathbf{E}_{\gamma,\rho}|_{x_2=\rho}\times\vec{n} = 0.
\end{aligned} \tag{8}$$

This modified truncated exterior problem is coupled to the interior problem using the modified matching conditions, c.f. (4)

$$(\mathbf{E} - (\mathbf{E}_{\gamma,\rho} + \mathbf{E}_{\mathrm{inc}}))\times\vec{n} = 0, \tag{9a}$$

$$(\varepsilon\mathbf{curl}_3\,\mathbf{E} - (\varepsilon_+\mathbf{curl}_{3,\gamma}\,\mathbf{E}_{\gamma,\rho} + \varepsilon_+\mathbf{curl}_3\,\mathbf{E}_{\mathrm{inc}}))\times\vec{n} = 0. \tag{9b}$$

3.2. Automatic adaption of the PML

As discussed in Sections 2.2 and 3.1 the PML method fails in the presence of anomalous modes. For an anomalous mode the field behaves like $\exp(\mathrm{i}(k_1x_1 + k_3x_3))$ and hence a complex continuation in x_2 direction does not make the complex continued field decay exponentially. To obtain an effective transparent boundary condition the very specific behavior in x_2 direction of the field is exploited. We propose a mixed *a priori* and *a*

posteriori refinement strategy of the PML method including the automatic adaption of the layer thickness ρ. The algorithm we propose was first published in [31]. We introduce a distance variable $\xi = |x_2 - x_{2,\pm}|$ and a tangential variable $\eta = x_1$ for the exterior domain. We assume the following expansion of the field in the exterior domain

$$\mathbf{u}(\eta, \xi) \sim \int \mathbf{c}(\eta, \alpha) \mathrm{e}^{\mathrm{i} k_\xi(\alpha)\xi} \mathrm{d}\alpha, \tag{10}$$

with $\mathrm{Re}\, k_\xi(\alpha) \geqslant 0$ and $\mathrm{Im}\, k_\xi(\alpha) \geqslant 0$. Hence in ξ direction the field is a superposition of outgoing or evanescent plane waves. In the periodic setting such an expansion is explicitly given in (5).

The complex continuation, $\xi \mapsto \gamma\xi$ with $\gamma = 1 + \mathrm{i}\sigma$, gives

$$\|\mathbf{u}_\gamma(\eta, \xi)\| \sim \int \|\mathbf{c}(\eta, \alpha)\| \mathrm{e}^{-\kappa\xi} \quad \text{with } \kappa = \sigma \mathrm{Re}\, k_\xi + \mathrm{Im}\, k_\xi. \tag{11}$$

The PML method only effects the outgoing part with $\mathrm{Re}\, k_\xi$ strictly larger than zero. Field contributions with a large $\mathrm{Re}\, k_\xi$ component are efficiently damped out. Evanescent field contributions are damped out independently of the complex continuation. For a proper approximation of the oscillatory and exponential behavior a discretization fine enough is needed to resolve the field. In contrast anomalous modes or "near anomalous" modes with $k_\xi \sim 0$ are neither evanescent nor damped out efficiently by the PML. Hence they enforce the usage of a large ρ but can be well approximated with a relatively coarse discretization in ξ due to their smoothness in ξ. These requirements are satisfied using an adaptive discretization. It is useful to think of the complex continuation as a high-frequency filter. With a growing distance ξ from the interior coupling boundary higher frequency contributions are damped out so that the discretization can be coarsened.

For a given tolerance ϵ selected according to the global accuracy requirements we introduce the cut-off function

$$\kappa_{\mathrm{co},\epsilon}(\xi) = -\ln(\epsilon)/\xi.$$

At any distance $\xi' > 0$ each component in the expansion (11) with $\kappa > \kappa_{\mathrm{co},\epsilon}(\xi')$ is damped out by a factor less than the threshold ϵ,

$$\mathrm{e}^{-\kappa\xi'} < \mathrm{e}^{-\kappa_{\mathrm{co},\epsilon,\epsilon}(\xi')\xi} = \mathrm{e}^{\ln(\epsilon)} = \epsilon.$$

Algorithm 1.

Adaptive PML method

Require $\epsilon, \sigma, h_{\mathrm{int}}, \kappa_{\min}$
  Compute $N_{\mathrm{p.w}}$ and $\xi_{\max}$ depending on
  h_{int} and finite element order
  while (not converged) **do**
    $\xi_0 = 0.0; \xi_1 = h_{\mathrm{int}}; N = 1;$
    while $(-\ln(\epsilon)/(\xi_N\sigma) < \kappa_{\min})$ **do**
      $\xi_{N+1} = \xi_N + \max\{h_{\mathrm{int}}, 2\pi\sigma\xi_N/(-\ln(\epsilon))/N_{\mathrm{p.w}}\}.$
      if $(\xi_{N+1} > 1/\epsilon)$ **then**
        break
      else
        $N = N + 1$
      end if
    end while
    Compute solution u with PML discretization $\{\xi_0, \xi_1, \ldots, \xi_N\}$
    if $\|u(\cdot, \xi_N)\| \leqslant \epsilon\|u(\cdot)\|$ **then**
      converged
    else if $\xi_N > \xi_{\max}$ **then**
      break
    else
      $\kappa_{\min} = \kappa_{\min}/2$
    end if
  end while

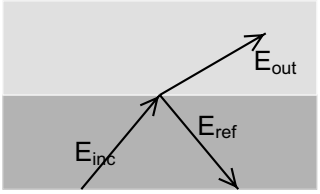

Fig. 2. Test problem for adaptive PML discretization. The lower material has an refractive index equal to $n_{\text{sub}} = 1.5$, the upper material block consists of air ($n_{\text{sup}} = 1.0$). By Snell's law the field is totally reflected for an incident angle equal to the *critical angle* $\vartheta_c = 180 \cdot \arcsin(1.0/1.5)/\pi \approx 41.81$.

Assuming that this damping is sufficient, we select a discretization which only needs to approximate the lower frequency parts with $\kappa \leqslant \kappa_{\text{co},\epsilon}(\xi)$ for $\xi > \xi'$. If a fixed number $N_{\text{p.w}}$ of discretization points per generalized wavelength $2\pi/\kappa$ is used, we obtain the following formula for the *a priori* determination of the local mesh width $h(\xi) = 2\pi\sigma/\kappa_{\text{co},\epsilon}(\xi)/N_{\text{p.w}}$. The choice of $N_{\text{p.w}}$ depends on the order of the finite element only, but not on the distance ξ, as the field is smooth in ξ-direction. As $\kappa_{\text{co},\epsilon}(\xi) \to \infty$ for $\xi \to 0$ the local mesh width is zero at $\xi = 0$. But as it is not reasonable to use a finer discretization in the exterior domain than in the interior domain, the local mesh width is bounded by the minimum mesh width h_{int} of the interior domain discretization on the coupling boundary,

$$h(\xi) = \max\{h_{\text{int}}, 2\pi\sigma/\kappa_{\text{co},\epsilon,\epsilon}(\xi)/N_{\text{p.w}}\}.$$

The parameters ϵ and $N_{\text{p.w}}$ are chosen to fit to the interior domain discretization quality. The grid $\{\xi_0, \xi_1, \xi_2, \ldots\}$ is recursively constructed by

$$\xi_{n+1} = \xi_n + h(\xi_n).$$

This way ξ_n grows exponentially with n. To truncate the grid we assume that components in the expansion with $\kappa < \kappa_{\min}$ can be neglected so that the grid $\{\xi_0, \xi_1, \ldots, \xi_N\}$ is determined by $\kappa_{\text{co},\epsilon,\epsilon}(\xi_N) < \kappa_{\min} \leqslant \kappa_{\text{co},\epsilon,\epsilon}(\xi_{N-1})$. In the periodic setting there exists such a $\kappa_{\min} > 0$ in case no anomalous mode is present.

As an *a posteriori* control we check if the field is indeed sufficiently damped out at ξ_N, $\|u(\cdot, \xi_N)\| \leqslant \epsilon\|u(\cdot)\|$.[3] Otherwise we recompute the solution with $\kappa_{\min} \to \kappa_{\min}/2$. Since for an anomalous mode the field is not damped at all we restrict the maximum ξ_N to $\xi_N < \pi/k_0/\epsilon$. The pseudocode of the algorithm is given in Algorithm 1. There ϵ is a given tolerance, that has to be estimated from the interior discretization, and h_{int} is the mesh-width of the boundary. The damping factor σ is fixed; $\sigma = 1$ is a good choice.

3.3. Validation on numerical experiments

To demonstrate the performance of the adaptive PML algorithm we compute the reflection of a plane wave at a material jump, c.f. Fig. 2. The angle of incidence varies from $\vartheta = 20°$ to $\vartheta = 60°$. The incoming field is rotated along the x_3 axis by an angle of 45°, so that the incidence is twofold oblique (conical). Hence the unit direction of the incoming field is equal to $(\cos 45° \sin\vartheta, \cos\vartheta, \sin 45° \sin\vartheta)$. The interior domain has a size of 1.5×1 in wavelength scales. To measure the error the field energy in the interior domain is computed and compared to the analytic value. In Fig. 3 the error is plotted for different refinement levels of the interior domain. The "+" line corresponds to the finest level. In Fig. 4 the automatically adapted thickness of the PML is plotted (left) and the number of discretization points N in ξ direction (right). As expected a huge layer is used at the critical angle, whereas the total number of discretization points remains moderate. As can be seen in Fig. 3 the maximum error appears at the critical angle. From that one may suspect a failure of the automatic PML adaption. But a closer analysis reveals that the chosen discretization in the PML layer is sufficient as can be seen from Table 1. There the thickness of the perfectly matched layer is fixed and the interior domain further refined. This way we observe convergence to the true solution. But the convergence rate is halved at the critical angle. Hence the maximum error at the critical angle comes from an insufficient interior

[3] Here we assume homogenous Neumann boundary conditions for the truncation of the PML layer. If homogenous Dirichlet boundary conditions are chosen for the truncation of the PML layer, the sufficient damping of the Neumann data may be checked instead.

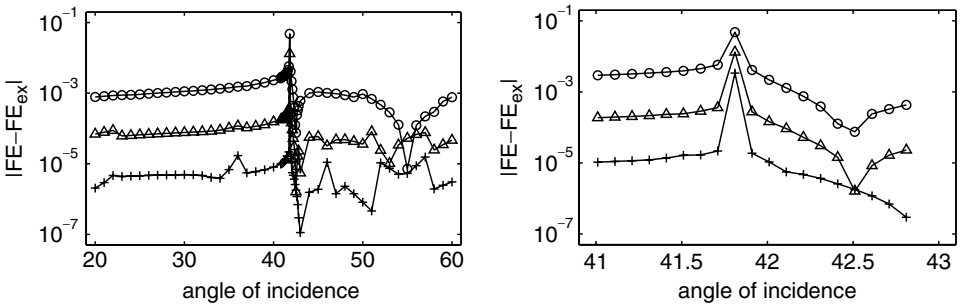

Fig. 3. Left: Field energy error in the interior domain. The three lines (○, △, +) corresponds to different refinement levels of the interior domain. Right: Zoom into left figure near critical angle.

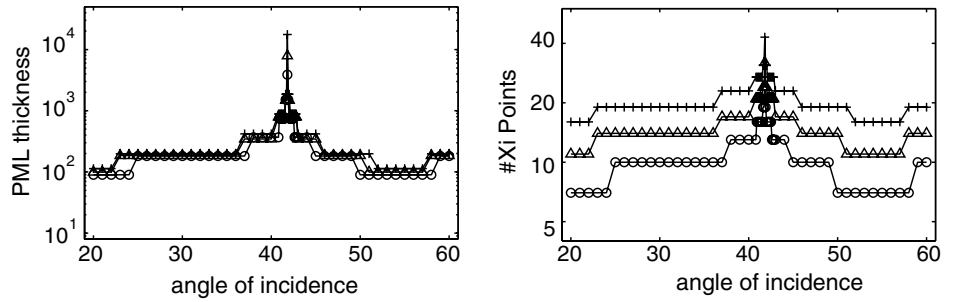

Fig. 4. Left: Thickness of the PML layer. At the critical angle the thickness is up to 10^4 times larger than the diameter of the interior domain. Right: Number of discretization points ξ_j used in the radial direction (x_2). Although the needed thickness of the layer is huge the number of unknowns used in the PML layer remains moderate.

discretization. We conjecture that this is due to a dispersion effect. Since the wave is traveling along the x_1 direction it reenters the periodic domain leading to large "path length".

4. Variational form

4.1. Derivation of the variational form

The coupled problem given by (8), (2) and (9) can be casted into a variational problem on the Sobolev space $H_{0,\rho}(\mathbf{curl}_3, \Omega \cup \Omega_\rho)$ of $H(\mathbf{curl}_3)$ fields with generalized zero Dirichlet values at $x_2 = \rho$.

For a given test function $\mathbf{\Phi} \in H_{0,\rho}(\mathbf{curl}_3, \Omega \cup \Omega_\rho)$ the following identity holds true:

Table 1
Convergence of field energy at critical angle of incidence

Step	ΔE	$\Delta E'$
0	0.359850	0.335129
1	0.159358	0.166207
2	0.048779	0.049502
3	0.012911	0.012912
4	0.003274	0.003266
5	0.000205	0.000820
6	0.000206	0.000205
7	0.000051	0.000051

The first column corresponds to the interior mesh refinement step. The relative error of the electric field energy in the interior domain is given in column two, $\Delta E = |\|\mathbf{E}_{\mathrm{ex}}\|^2_{L^2} - \|\mathbf{E}_h\|^2_{L^2}|/\|\mathbf{E}_{\mathrm{ex}}\|^2_{L^2}$. In column three the relative error of the magnetic field energy $\Delta E' = |\|\mathbf{curl}\,\mathbf{E}_{\mathrm{ex}}\|^2_{L^2} - \|\mathbf{curl}\,\mathbf{E}_{\mathbf{h}}\|^2_{L^2}|/\|\mathbf{curl}\,\mathbf{E}_{\mathrm{ex}}\|$ is given. For fixed PML thickness the solution converges as the interior mesh is refined.

$$\gamma \int_{\Omega_\rho} \overline{\mathbf{\Phi}} \cdot \mathbf{curl}_{3,\gamma}\, \mu^{-1} \mathbf{curl}_{3,\gamma}\, \mathbf{E}_\gamma,$$
$$\gamma \int_{\Omega_\rho} \overline{\mathbf{curl}_{3,\gamma}\, \mathbf{\Phi}} \cdot \mu^{-1} \mathbf{curl}_{3,\gamma}\, \mathbf{E}_\gamma - \int_{x_2=0} \overline{\mathbf{\Phi}} \cdot \mu^{-1} \mathbf{curl}_3\, \mathbf{E}_{\mathrm{sc}} \times \vec{n}, \tag{12}$$

where $\mathbf{E}_\gamma(x_1,x_2,x_3) = \mathbf{E}_{\mathrm{sc}}(x_1,\gamma x_2,x_3)$, c.f. (7). We first proof this identity for $\gamma \in \mathbb{R}\setminus\{0\}$. Using the non-euclidian coordinate change

$$\mathrm{T}^{-1} : (x_1,x_2,x_3) \mapsto (x_1,\gamma^{-1}x_2,x_3)$$

and applying the transformation rules for differential forms, see [29], one gets

$$\int_{\Omega_{\gamma\rho}} \overline{\mathbf{\Phi}^*} \cdot \mathbf{curl}_3\, \mu^{-1} \mathbf{curl}_3\, \mathbf{E}_{\mathrm{sc}} = \int_{\Omega_\rho} \overline{\mathbf{\Phi}_*} \cdot \mathbf{curl}_3\, \mu_*^{-1} \mathbf{curl}_3\, \mathbf{E}_*, \tag{13a}$$
$$\int_{\Omega_{\gamma\rho}} \overline{\mathbf{curl}_3\, \mathbf{\Phi}^*} \cdot \mu^{-1} \mathbf{curl}_3\, \mathbf{E}_{\mathrm{sc}} = \int_{\Omega_\rho} \overline{\mathbf{curl}_3\, \mathbf{\Phi}_*} \cdot \mu_*^{-1} \mathbf{curl}_3\, \mathbf{E}_*, \tag{13b}$$

with

$$\mu_* = |J| J^{-1} \mu J^{-\mathrm{t}}, \tag{14a}$$
$$\mathbf{E}_*(x_1,x_2,x_3) = J^{\mathrm{t}} \mathbf{E}_{\mathrm{sc}}(x_1,\gamma x_2,x_3), \tag{14b}$$
$$\mathbf{\Phi}_*(x_1,x_2,x_3) = J^{\mathrm{t}} \mathbf{\Phi}(x_1,x_2,x_3) = J^{\mathrm{t}} \mathbf{\Phi}^*(x_1,\gamma x_2,x_3). \tag{14c}$$

$J = \mathrm{diag}(1,\gamma,1)$ is the constant Jacobian of T. Note that $\mathbf{\Phi}_*$, $\mathbf{E}_*$ are the pulled back fields to $\mathbf{\Phi}^*$ and $\mathbf{E}_{\mathrm{sc}}$ in the sense of differential form calculus.

We have

$$\gamma \int_{\Omega_\rho} \overline{\mathbf{\Phi}} \cdot \mathbf{curl}_{3,\gamma}\, \mu^{-1} \mathbf{curl}_{3,\gamma}\, \mathbf{E}_\gamma = \int_{\Omega_\rho} \overline{\mathbf{\Phi}_*} \cdot \mathbf{curl}_3\, \mu_*^{-1} \mathbf{curl}_3\, \mathbf{E}_*, \tag{15a}$$
$$\gamma \int_{\Omega_\rho} \overline{\mathbf{curl}_{3,\gamma}\, \mathbf{\Phi}} \cdot \mu^{-1} \mathbf{curl}_{3,\gamma}\, \mathbf{E}_\gamma = \int_{\Omega_\rho} \overline{\mathbf{curl}_3\, \mathbf{\Phi}_*} \cdot \mu_*^{-1} \mathbf{curl}_3\, \mathbf{E}_*, \tag{15b}$$

which is verified by inserting (14) and using $\mathbf{curl}_{3,\gamma} = |J|^{-1} J \mathbf{curl}_3 J^{\mathrm{t}}$.

On the other hand integration by parts yields

$$\int_{\Omega_\rho} \overline{\mathbf{\Phi}_*} \cdot \mathbf{curl}_3\, \mu_*^{-1} \mathbf{curl}_3\, \mathbf{E}_* = \int_{\Omega_\rho} \overline{\mathbf{curl}_3\, \mathbf{\Phi}_*} \cdot \mu_*^{-1} \mathbf{curl}_3\, \mathbf{E}_* - \int_{x_2=0} \overline{\mathbf{\Phi}_*} \cdot (\mu_*^{-1} \mathbf{curl}_3\, \mathbf{E}_* \times \vec{n}) \tag{16}$$

and a respective equation for $\mathbf{E}_{\mathrm{sc}}$, μ, and $\mathbf{\Phi}^*$ with the domain of integration $\Omega_{\gamma\rho}$. These together with equations in (13) give

$$\int_{x_2=0} \overline{\mathbf{\Phi}_*} \cdot (\mu_*^{-1} \mathbf{curl}_3\, \mathbf{E}_* \times \vec{n}) = \int_{x_2=0} \overline{\mathbf{\Phi}^*} \cdot (\mu^{-1} \mathbf{curl}_3\, \mathbf{E}_{\mathrm{sc}} \times \vec{n}). \tag{17}$$

Using that $\mathbf{E}_\gamma = J^{-\mathrm{t}} \mathbf{E}_*$ and using that the tangential components of $\mathbf{\Phi}^*$ are equal to $\mathbf{\Phi}$, one derives from (15) and (17) the desired identity (12) for real γ. Since each term is a holomorphic function in γ the identity (12) holds true for $\gamma \in \mathbb{C}\setminus\{0\}$.

The coupled problem given by (8), (2) and (9) in weak form is given by

$$\int_\Omega \overline{\mathbf{curl}_3\, \mathbf{\Phi}} \cdot \mu^{-1} \mathbf{curl}_3\, \mathbf{E} - \omega^2 \overline{\mathbf{\Phi}} \cdot \varepsilon \mathbf{E} + \gamma \int_{\Omega_\rho} \overline{\mathbf{curl}_{3,\gamma}\, \mathbf{\Phi}} \cdot \mu^{-1} \mathbf{curl}_{3,\gamma}\, \mathbf{E}_\gamma - \omega^2 \overline{\mathbf{\Phi}} \cdot \varepsilon \mathbf{E}_\gamma$$
$$= - \int_{x_2=0} \overline{\mathbf{\Phi}} \cdot \mu^{-1} (\mathbf{curl}_3\, \mathbf{E} - \mathbf{curl}_3\, \mathbf{E}_{\mathrm{sc}}) \times \vec{n}. \tag{18}$$

Due to the Neumann coupling condition $\mathbf{curl}_3\, \mathbf{E} \times \vec{n} = \mathbf{curl}_3\, \mathbf{E}_{\mathrm{sc}} \times \vec{n} + \mathbf{curl}_3\, \mathbf{E}_{\mathrm{inc}} \times \vec{n}$ the boundary term is equal to $\int_{x_2=0} \mathbf{\Phi} \cdot \mu^{-1} \mathbf{curl}_3\, \mathbf{E}_{\mathrm{inc}} \times \vec{n}$. This is not yet the basis for a Galerkin ansatz in $H_{0,\rho}(\mathbf{curl}_3, \Omega \cup \Omega_\rho)$ as there is a jump of the Dirichlet data across the boundary $x_2 = 0$, precisely $\mathbf{E}_\gamma + \mathbf{E}_{\mathrm{inc}} = \mathbf{E}|_{x_2=0}$. Let

$\Pi(\mathbf{E}_{\text{inc}} \times \vec{n}) \in H_{0,\rho}(\mathbf{curl}_3, \Omega_\rho)$ denote an extension of a field with tangential Dirichlet data equal to $\mathbf{E}_{\text{inc}} \times \vec{n}$ at $x_2 = 0$ to $H_{0,\rho}(\mathbf{curl}_3, \Omega_\rho)$ and add this to $\mathbf{E}_\gamma$ to obtain

$$\int_\Omega \overline{\mathbf{curl}_3 \boldsymbol{\Phi}} \cdot \mu^{-1} \mathbf{curl}_3 \mathbf{E} - \omega^2 \overline{\boldsymbol{\Phi}} \cdot \varepsilon \mathbf{E} + \gamma \int_{\Omega_\rho} \overline{\mathbf{curl}_{3,\gamma} \boldsymbol{\Phi}} \cdot \mu^{-1} \mathbf{curl}_{3,\gamma} (\mathbf{E}_\gamma + \Pi(\mathbf{E}_{\text{inc}} \times \vec{n})) - \omega^2 \overline{\boldsymbol{\Phi}} \cdot \varepsilon (\mathbf{E}_\gamma + \Pi(\mathbf{E}_{\text{inc}} \times \vec{n}))$$
$$= - \int_{x_2=0} \overline{\boldsymbol{\Phi}} \cdot \mu^{-1} (\mathbf{curl}_3 \mathbf{E}_{\text{inc}} \times \vec{n}) + \gamma \int_{\Omega_\rho} \overline{\mathbf{curl}_{3,\gamma} \boldsymbol{\Phi}} \cdot \mu^{-1} \mathbf{curl}_{3,\gamma} \Pi(\mathbf{E}_{\text{inc}} \times \vec{n}) - \omega^2 \overline{\boldsymbol{\Phi}} \cdot \varepsilon \Pi(\mathbf{E}_{\text{inc}} \times \vec{n}). \tag{19}$$

This motivates the definition of the composed field $\mathbf{u} \in H_{0,\rho}(\mathbf{curl}_3, \Omega \cup \Omega_\rho)$ by $\mathbf{u}|_\Omega = \mathbf{E}$ and $\mathbf{u}|_{\Omega_\rho} = \mathbf{E}_{\text{sc}} + \Pi(\mathbf{E}_{\text{inc}} \times \vec{n})$ and of the following bilinear form:

$$a(\boldsymbol{\Phi}, \mathbf{u}) := a_\Omega(\boldsymbol{\Phi}|_\Omega, \mathbf{u}|_\Omega) + a_{\Omega_\rho}(\boldsymbol{\Phi}|_{\Omega_\rho}, \mathbf{u}|_{\Omega_\rho}), \tag{20}$$

with

$$a_\Omega(\boldsymbol{\Phi}, \mathbf{u}) := \int_\Omega \overline{\mathbf{curl}_3 \boldsymbol{\Phi}} \cdot \mu^{-1} \mathbf{curl}_3 \mathbf{u} - \omega^2 \overline{\boldsymbol{\Phi}} \cdot \varepsilon \mathbf{u}, \tag{21}$$

$$a_{\Omega_\rho}(\boldsymbol{\Phi}, \mathbf{u}) := \gamma \int_{\Omega_\rho} \overline{\mathbf{curl}_{3,\gamma} \boldsymbol{\Phi}} \cdot \mu^{-1} \mathbf{curl}_{3,\gamma} \mathbf{u} - \omega^2 \overline{\boldsymbol{\Phi}} \cdot \varepsilon \mathbf{u}. \tag{22}$$

Defining

$$b_\Gamma(\boldsymbol{\Phi}, \boldsymbol{\Psi}) := \int_\Gamma \overline{\boldsymbol{\Phi}} \cdot \mu^{-1} \boldsymbol{\Psi} \tag{23}$$

we end up with the variational problem: find $\mathbf{u} \in H_{0,\rho}(\mathbf{curl}_3, \Omega \cup \Omega_\rho)$ such that for all $\boldsymbol{\Phi} \in H_{0,\rho}(\mathbf{curl}_3, \Omega \cup \Omega_\rho)$

$$a(\boldsymbol{\Phi}, \mathbf{u}) = a_{\Omega_\rho}(\boldsymbol{\Phi}, \Pi(\mathbf{E}_{\text{inc}} \times \vec{n})) - b_\Gamma(\boldsymbol{\Phi}, \mathbf{curl}_3 \mathbf{E}_{\text{inc}} \times \vec{n}). \tag{24}$$

Here we have avoided the definition of a DtN-operator. The total field is calculated as the solution of a coupled system (computational domain coupled to the PML), where the Dirichlet and Neumann data enter the equation on the "right-hand side". If $\mathbf{u}$ is a solution of Maxwell's equations (1), the integration by parts identity can be rewritten using these bilinear forms as

$$a_\Omega(\boldsymbol{\Phi}, \mathbf{u}) - b(\boldsymbol{\Phi}, -\mathbf{curl}_3 \mathbf{u} \times \vec{n}) = 0. \tag{25}$$

This formula will be useful to represent the Neumann data. Note that in (25) $\vec{n}$ is the "inward" normal with respect to Ω.

4.2. Finite element discretization

To discretize the variational problem (24) we use vectorial finite elements on a triangular mesh in the interior domain and on a quadrilateral mesh in the PML. The three sub-meshes – lower PML mesh, interior domain mesh and upper PML mesh – fit non-overlapping. In the PML we use a rectangular mesh $[0, x_{1,2}, \ldots, a] \times [x_{2,+}, x_{2,+} + \xi_1, \ldots, x_{2,+} + \xi_N]$ where $\xi_1, \ldots, \xi_N$ are determined as described in Section 3.2. Since the Sobolev space $H_{0,\rho}(\mathbf{curl}_3, \Omega \cup \Omega_\rho)$ is isomorphic to $H_{0,\rho}(\mathbf{curl}_{2\text{D}}, \Omega \cup \Omega_\rho) \times H^1_{0,\rho}(\Omega \cup \Omega_\rho)$ with the two dimensional **curl** operator $\mathbf{curl}_{2\text{D}}(u_1, u_2) = \partial_{x_1} u_2 - \partial_{x_2} u_1$ we use higher order Whitney elements to discretize the first and second component of the electric field and standard Lagrange elements for the third field component of the same order.

Bloch periodicity is enforced by a multiplication of basis functions associated with one of two corresponding periodic boundaries of the domain by the Bloch factor, c.f. [4]. An interior edge element function remains unchanged, c.f. Fig. 5 (left). The support of a basis function associated with a periodic edge on the boundary consists of two triangles, c.f. Fig. 5 (right). The restriction of the basis function to the left triangle is defined as the standard shape function, whereas the shape-function on the right triangle is multiplied by the Bloch factor $\exp(\mathrm{i} k_1 a)$. The construction of Bloch periodic Lagrange elements is similar.

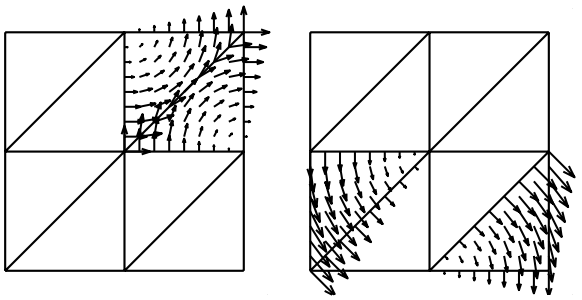

Fig. 5. First order edge elements on a simple grid. In the interior the tangential component is continuous across element boundaries. At the Bloch periodic boundary there is a phase shift.

5. Domain decomposition method

The idea for the Schwarz algorithm with transparent boundary conditions at the interfaces is to calculate the solution on every sub-domain separately using transparent boundary conditions and iteratively add the scattered field of each sub-domain to the incoming field for the neighboring sub-domains. The presentation here is restricted to the multiplicative (Gauß-Seidel) Schwarz-algorithm.

In its general form the domain-decomposition algorithm is given in (26). There $\mathbf{E}_j^n$ denotes the nth iterate on sub-domain Ω_j. $\Omega_{j,\rho,i}$ is the PML domain to Ω_j at the interface to Ω_i; $\Omega_{j,\rho}$ denotes the PML domain to Ω_j at the interface to the exterior, c.f. Fig. 6. The sub-domains are arranged linearly.

$$
\begin{aligned}
&\text{set } \mathbf{E}_j^0 = 0 \text{ for all } j\\
&\text{while not converged}\\
&\quad \text{for all sub-domains } j\\
&\qquad \text{find } \mathbf{E}_j^n \text{ such that}\\
&\qquad a_j(\mathbf{\Phi}, \mathbf{E}_j^n) = a_{\Omega_{j,\rho}}(\mathbf{\Phi}, \Pi(\mathbf{E}_{\text{inc}} \times \vec{n})) - b_{\Gamma_j}(\mathbf{\Phi}, \mathbf{curl}_3\, \mathbf{E}_{\text{inc}} \times \vec{n})\\
&\qquad + a_{\Omega_{j,\rho,j-1}}(\mathbf{\Phi}, \Pi(\mathbf{E}_{j-1}^n \times \vec{n})) - b_{\Gamma_{j,j-1}}(\mathbf{\Phi}, \mathbf{curl}_3\, \mathbf{E}_{j-1}^n \times \vec{n})\\
&\qquad + a_{\Omega_{j,\rho,j+1}}(\mathbf{\Phi}, \Pi(\mathbf{E}_{j+1}^{n-1} \times \vec{n})) - b_{\Gamma_{j,j+1}}(\mathbf{\Phi}, \mathbf{curl}_3\, \mathbf{E}_{j+1}^{n-1} \times \vec{n})\\
&\qquad \forall \mathbf{\Phi} \in H_{0,\rho}(\mathbf{curl}_3, \Omega_j \cup \Omega_{j,\rho} \cup_{i\in\{j-1,j+1\}} \Omega_{j,\rho,i}).
\end{aligned}
\tag{26}
$$

This algorithm requires the evaluation of Neumann data $\mathbf{curl}_3 \mathbf{E}_i \times \vec{n}$ along the boundary. Each sub-domain has only two well separated boundaries neglecting the periodic boundary and at most two neighboring domains. Inserting an additional post-processing step, the Neumann-data can be evaluated weakly.

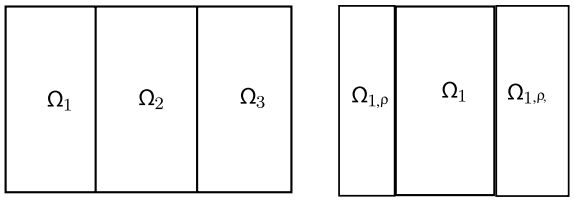

Fig. 6. Schematic sketch of the various domains and PMLs. Left: The computational domain Ω is split in three sub-domains. Right: The sub-domain Ω_1, with its two PMLs. Top and lower boundary are periodic boundaries.

$$
\begin{aligned}
&\text{set } \mathbf{E}_j^0 = 0 \text{ for all } j\\
&\text{while not converged}\\
&\quad \text{for all sub-domains } j\\
&\qquad \text{find } \mathbf{E}_j^n \text{ such that}\\
&\qquad a_j(\mathbf{\Phi}, \mathbf{E}_j^n) = +a_{\Omega_{j,\rho}}(\mathbf{\Phi}, \Pi(\mathbf{E}_{\text{inc}} \times \vec{n})) - b_{\Gamma_j}(\mathbf{\Phi}, \mathbf{curl}_3\, \mathbf{E}_{\text{inc}} \times \vec{n})\\
&\qquad + a_{\Omega_{j,\rho,j-1}}(\mathbf{\Phi}, \Pi(\mathbf{E}_{j-1}^n \times \vec{n})) - b_{\Gamma_{j,j-1}}(\mathbf{\Phi}, \mathbf{curl}_3\, \mathbf{E}_{j-1}^n \times \vec{n})\\
&\qquad + a_{\Omega_{j,\rho,j+1}}(\mathbf{\Phi}, \Pi(\mathbf{E}_{j+1}^{n-1} \times \vec{n})) - b_{\Gamma_{j,j+1}}(\mathbf{\Phi}, \mathbf{curl}_3\, \mathbf{E}_{j+1}^{n-1} \times \vec{n})\\
&\qquad \forall \mathbf{\Phi} \in H_{0,\rho}(\mathbf{curl}_3, \Omega_j \cup \Omega_{j,\rho} \cup_{i\in\{j-1,j+1\}} \Omega_{j,\rho,i});\\
&\quad \text{for all sub-domains } j\\
&\qquad b_{\Gamma_{j,j+1}}(\mathbf{\Phi}, \mathbf{curl}_3\, \mathbf{E}_j^n \times \vec{n}) + b_{\Gamma_{j,j-1}}(\mathbf{\Phi}, \mathbf{curl}_3\, \mathbf{E}_j^n \times \vec{n})\\
&\qquad + b_{\Gamma_j}(\mathbf{\Phi}, \mathbf{curl}_3\, \mathbf{E}_{\text{inc}} \times \vec{n}) = -a_{\Omega_j}(\mathbf{\Phi}, \mathbf{E}_j^n)
\end{aligned}
\tag{27}
$$

In order to distinguish $b_{\Gamma_{j,j-1}}(\mathbf{\Phi}, \mathbf{curl}_3\, \mathbf{E}_j^n \times \vec{n})$ from $b_{\Gamma_{j,j+1}}(\mathbf{\Phi}, \mathbf{curl}_3\, \mathbf{E}_j^n \times \vec{n})$, it is required that there are no test functions that have a support in elements adjacent to $\Gamma_{j,j+1}$ and $\Gamma_{j,j-1}$ simultaneously.

5.1. Schwarz algorithm for EUV

For the special application – scattering off an EUV-line mask – one can make use of the "simple" geometry of the multilayer stack that serves as a mirror employing the Transfer Matrix algorithm of Section 2.4. A simple situation is depicted in Fig. 7. The upper domain contains the mask line whereas the lower domain consists of the multilayer stack and the lower substrate block. Instead of solving Maxwell's equations by the finite element method in the multilayer stack, the incoming field is Fourier transformed and for each Fourier mode the Transfer Matrix algorithm is used to calculate the scattered field. This can even be simplified. If the tangential component of each Fourier-mode vector field is written as the linear combination of two linear independent polarizations, it is sufficient to compute the reflection coefficients of the multilayer stack for each mode and each polarization only once. The number of Fourier mode ranges from $n_{\min}$ to $n_{\max}$. To determine these, we set $k_{\max} = 0.1 \cdot 2\pi/h_{\max}$, where $h_{\max}$ is the maximum segment size of a finite element at the boundary. Then $n_{\max}$ is the greatest integer such that $k_1 + n_{\max} 2\pi/a < k_{\max}$, i.e. and $n_{\min}$ is the greatest integer, such that $k_x - n_{\min} 2\pi/a > -k_{\max}$.

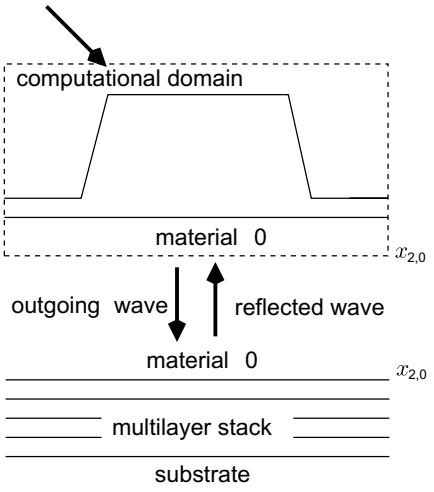

Fig. 7. Decomposition of the problem into two infinite sub-domains. The scattering problem is solved by the Finite Element Method in the upper domain and quasi-analytically in the lower domain.

6. Numerical examples

Two numerical examples are presented below. For one further example see [30]. In [21] the domain decomposition algorithm described above is applied to study the influence of shape and material parameters of EUV masks.

6.1. An academic example

The simple geometry of this example is depicted in Fig. 8. It consists of three domains Ω_1 and Ω_2, each with a quadrilateral material inhomogeneity and Ω_3 a layer stack of four layers below Ω_2. The period is $a = 1$. The different shadings correspond to different materials as indicated. The permeability is equal to $+1$ everywhere. The permittivity is given by $\varepsilon_1 = 1.01$, $\varepsilon_2 = 1.52$, $\varepsilon_3 = 1.03$, $\varepsilon_4 = 1.54$, $\varepsilon_5 = 1.55$, $\varepsilon_6 = 1.06$, $\varepsilon_7 = 1.57$, $\varepsilon_8 = 1.08$. The semi-infinite top and lower strips, with refraction indices $\varepsilon_9 = 1$ and $\varepsilon_0 = 1$ are not shown. These are completely modeled by the PML method. The incoming field is a plane waves with wave vector $\vec{k}_{\text{inc}} = (1, -2, 1)$ and wave length, $\lambda = 0.84$. The strength is $\vec{s}_{\text{inc}} = (1, 1, 1) \times \vec{k}_{\text{inc}} / \|(1, 1, 1) \times \vec{k}_{\text{inc}}\|$.

In the experiment the relative error is measured against the discrete solution obtained by solving the scattering problem on the whole domain. In solving the scattering problem on the whole domain, the PML is chosen adaptively. These PML parameters are then fixed and used for all sub-domains. Three cases are distinguished.

(1) Schwarz algorithm with two domains (D2): One domain is Ω_1 and the second domain is the union of Ω_2 and Ω_3. Thus the layers are discretized by finite elements. In the convergence plot of Fig. 8 this corresponds to the dark gray lines.
(2) Schwarz algorithm with two domains (D2-EUV): One domain is Ω_1, the second domain is Ω_2. Ω_3 the layer stack is treated analytically and is like a boundary condition for Ω_2. That is, if the subproblem on Ω_2 is solved we iterate internally between Ω_2 and Ω_3 and stop if the error is below 10^{-9} or after at most 100 iterations. In the domain decomposition algorithm only the number of iterations between Ω_1 and Ω_2 is counted. In the convergence plot of Fig. 8 this corresponds to the black lines.
(3) Schwarz algorithm with three domains (D3): We are using a multiplicative Schwarz algorithm with three sub-domains. Within one "iteration cycle", we first solve for $\mathbf{E}_1$, then for $\mathbf{E}_2$ and finally for $\mathbf{E}_3$. On each sub-domain the finite element method is used. In the convergence plot of Fig. 8 this corresponds to the light gray lines.

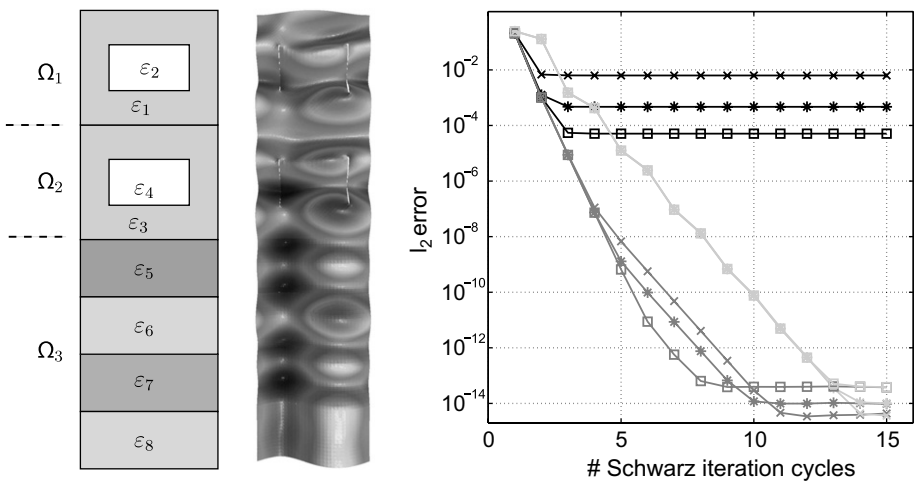

Fig. 8. Material distribution (left) and magnitude of the electric field (middle) for a simple test problem. Convergence plot (right) for $\vec{k}_{\text{inc}} = (1, -2, 1)$, $\lambda = 0.84$ and different refinement levels.

For these three cases the error versus the number of Schwarz iteration cycles is shown in Fig. 8 (right). The experiment is performed for three different refinement levels, where " × " corresponds to the coarsest level with 6496 degrees of freedom on the whole domain including the PML; sub-domain Ω_1 has 3328, Ω_2 has 2752, Ω_3 has 2552 and $\Omega_2 \cup \Omega_3$ 4352 degrees of freedom including the PML in the first iteration loop.

The next finer level labeled with "∗" is obtained by one uniform refinement of the initial grid and has 24,384 degrees of freedom. The finest level (92,032 degrees of freedom) labeled with "□" is obtained by two uniform refinements of the initial grid. In each case second order finite elements are used. In case (D2-EUV) the error saturates at a level that clearly depends on the refinement of the interior grid. This behavior can be expected as the number of Fourier coefficients that are taken into account to couple the layer-stack analytically in the Schwarz iteration is inverse proportional to the mesh-width. In case (D2) and (D3) the error saturates at $1e{-}14$, which is close to machine precision. This surprisingly good convergence behavior will be further analyzed in a subsequent paper. The geometry, the permittivity and the angle of incidence all influence the convergence.

6.2. Real life EUV mask

A schematic sketch of a more realistic EUV line mask is shown in Fig. 9. There only four out of ten MoSi double layers are shown. The periodicity a is 40 nm. The line made of silicon (Si) and the chromium absorber (Cr) have a width of 20 nm and a height of 15 nm. The first silicon layer's height is 10 nm. Each molybdenum layer (Mo) has a height of 6 nm and the subsequent silicon layers have a height of 8 nm. The wavelength is 14 nm. The permeability is 1.0 everywhere. The permittivities are $\varepsilon_{\mathrm{Mo}} = 1.69 + 0.016i$, $\varepsilon_{\mathrm{Si}} = 1.21 + 0.002i$, $\varepsilon_{\mathrm{Cr}} = 1.43 + 0.24i$ and $\varepsilon_{\mathrm{Air}} = 1.0$.

Starting from a coarse mesh the grid is pre-refined to have at least 3, 4, 5, 6, 7, 8, 9, 16 and 20 points per wavelength locally. The solution obtained with 20 points per wavelength is taken as a reference solution to measure the error.

We use a domain decomposition algorithm and decompose the mask into Ω_1 (line, absorber, air) and Ω_2 (multilayer stack). The multilayer stack is treated analytically as described in Section 5.1. Additionally we are using a damping factor of 0.66 in the domain decomposition algorithm to speed up convergence.

The PML is chosen adaptively as described in Section 3.2.

Fig. 9 (middle) shows the error versus the number of degrees of freedom in the finite element grid including the PML. To obtain the solid line, the multilayer stack is discretized using finite elements. Clearly, if the multilayer stack is not discretized, but treated analytically and coupled to Ω_1 in the domain-decomposition algorithm, the number of degrees of freedom is reduced drastically. The above calculations where performed on an *AMD Opteron PC* with 32 GB of RAM. The arising linear systems are solved with the sparse direct solver *PARDISO* [24,25]; *PARDISO* shows a nice linear dependency between the size of the problem and the

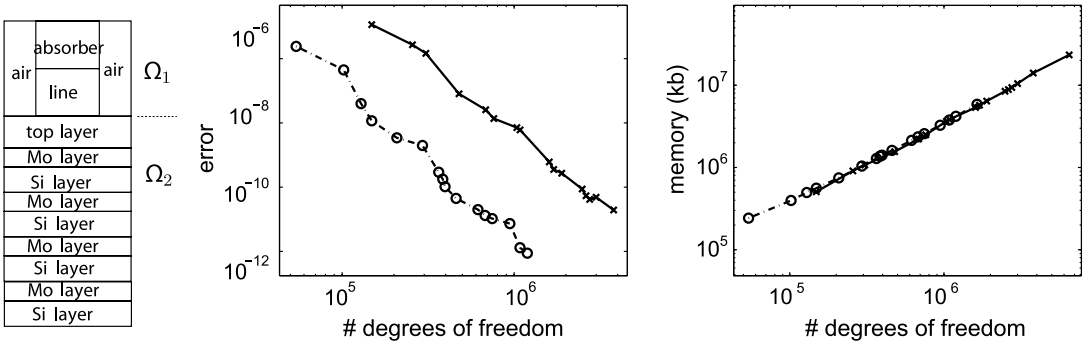

Fig. 9. Left: Sketch of an EUV line mask. Middle: Error versus the number of degrees of freedom in finite element mesh. The dashed error curve is obtained using the domain decomposition algorithm, decomposing the computational domain in two sub-domains (the line and the multilayer stack) and treating the multilayer stack separately. The solid error curve is obtained discretizing the whole computational domain. Right: Total memory required in (kb) versus the number of degrees of freedom. The sparse direct solver *PARDISO* shows a nice linear dependency between problem size and memory complexity.

memory required. This reduction of the number of degrees of freedom due to the domain decomposition approach, allows to compute realistic masks on standard 32-bit computers.

Acknowledgement

We thank one anonymous referee, who pointed out that the problem may not only be ill posed due to the radiation condition at infinity but due to the existence of guided waves, c.f. Section 2.3.

References

[1] J.-D. Benamou, B. Després, A domain decomposition method for the Helmholtz equation and related optimal control problems, J. Comput. Phys. 136 (1) (1997) 68–82.
[2] J.-P. Bérenger, A perfectly matched layer for the absorption of electromagnetic waves, J. Comput. Phys. 114 (2) (1994) 185–200.
[3] M. Born, E. Wolf, Principles of Optics, Cambridge University Press, 1999.
[4] S. Burger, R. Klose, A. Schädle, F. Schmidt, L. Zschiedrich, Adaptive FEM solver for the computation of electromagnetic eigenmodes in 3d photonic crystal structures, in: Proc. Sci. Comp. Electr. Eng. 2004, 2005.
[5] S. Burger, R. Köhle, L. Zschiedrich, W. Gao, F. Schmidt, R. März, C. Nölscher, Benchmark of FEM waveguide and FDTD algorithms for rigorous mask simulation, in: J.T. Weed, P.M. Martin (Eds.), Photomask Technology, vol. 5992, SPIE, Bellingham, Washington, USA, 2005, pp. 368–379.
[6] X.-C. Cai, M.A. Casarin, F.W. jun. Elliott, O.B. Widlund, Overlapping Schwarz algorithms for solving Helmholtz's equation, in: J. Mandel, et al. (Eds.), Domain decomposition methods 10, Contemp. Math., vol. 218, AMS, Providence, RI, 1998, pp. 391–399.
[7] F. Collino, S. Ghanemi, P. Joly, Domain decomposition methods for harmonic wave propagation: a general presentation, Comput. Methods Appl. Mech. Engrg. 184 (2000) 171–211.
[8] F. Collino, P. Monk, The perfectly matched layer in curvilinear coordinates, SIAM J. Sci. Comput. (1998).
[9] A. de La Bourdonnaye, Ch. Farhat, A. Macedo, F. Magoulés, F.-X. Roux, A non overlapping domain decomposition method for the exterior Helmholtz problem, Technical Report 3271, INRIA, 1997.
[10] B. Després, Décomposition de domaine et probléme de Helmholtz, C.R. Acad. Sci., Paris, Sér I 311 (6) (1990) 313–316.
[11] J. Elschner, R. Hinder, F. Penzel, G. Schmidt, Existence, uniqueness and regularity for solutions of the conical diffraction problem, Math. Models Methods Appl. Sci. 10 (2000) 317–341.
[12] J. Elschner, R. Hinder, G. Schmidt, Finite element solution of conical diffraction problems, Adv. Comput. Math. 16 (2002) 139–156.
[13] J.M. Gander, F. Magoulés, F. Nataf, Optimized Schwarz methods without overlap for the Helmholtz equation, J. Sci. Comput. 24 (1) (2002) 38–60.
[14] S. Ghanemi, A domain decomposition method for Helmholtz scattering problems, in: Ninth International Conference on Domain Decomposition Methods, DDM.org, 1998, pp. 105–112.
[15] T. Hohage, F. Schmidt, L. Zschiedrich, Solving time-harmonic scattering problems based on the pole condition II: convergence of the PML method, SIAM J. Math. Anal. 35 (3) (2003) 547–560.
[16] M. Lassas, E. Somersalo, On the existence and convergence of the solution of PML equations, Computing 60 (3) (1998) 229–241.
[17] M. Lassas, E. Somersalo, Analysis of the PML equations in general convex geometry, Proc. Roy. Soc. Edinburgh Sect. A 131 (5) (2001) 1183–1207.
[18] S.-Ch. Lee, M.N. Vouvakis, J-F. Lee, A non-overlapping domain decomposition method with non-matching grids for modeling large finite antenna arrays, J. Comp. Phys. (203) (2005) 1–21.
[19] R. Petit, Electromagnetic Theory of Gratings, Springer-Verlag, 1980.
[20] L. Plattner, A study in biomimetics: nanometer-scale, high-efficiency, dielectric diffractive structures on the wings of butterflies and in the silicon chip factory, Ph.D. thesis, School of Electronics and Computer Science, University of Southampton, 2003. <http://eprints.ecs.soton.ac.uk/10031/>.
[21] J. Pomplun, S. Burger, F. Schmidt, L. Zschiedrich, F. Scholze, Rigorous FEM-simulation of EUV-masks: influence of shape and material parameters, in: P.M. Martin, R.J. Naber (Eds.), Photomask Technology, vol. 6349, SPIE, Bellingham, Washington, USA, 2006, p. 63493D.
[22] A.A. Rodríguez, L. Gerardo-Giorda, New nonoverlapping domain decomposition methods for the harmonic Maxwell system, SIAM J. Sci. Comput. 28 (1) (2006) 102–122.
[23] A. Schädle, L. Zschiedrich, Additive Schwarz method for scattering problems using the PML method at interfaces, in: O.B. Widlung, D.E. Keyes (Eds.), Domain Decomposition Methods in Science and Engineering XVI, Lecture Notes in Computational Science and Engineering, vol. 55, Springer, 2007, pp. 205–212.
[24] O. Schenk, K. Gärtner, On fast factorization pivoting methods for sparse symmetric indefinite systems, Electronic Transactions on Numerical Analysis 23 (2006) 158–179.
[25] O. Schenk, K. Gärtner, Solving unsymmetric sparse systems of linear equations with PARDISO, J. Future Generation Comput. Syst. 20 (3) (2004) 475–487.
[26] K. Schuster, Anwendung der Vierpoltheorie auf die Probleme der optischen Reflexionsminderung, Reflexionsverstärkung und der Interferenzfilter, Ann. der Physik, VI.F. 4 (1949) 352–356.

[27] V.V. Shaidurov, E.I. Ogorodnikov, Some numerical method of solving Helmholtz wave equation, in: G. Cohen, L. Halpern, P. Joly (Eds.), Mathematical and Numerical Aspects of Wave Propagation Phenomena, SIAM, 1991, pp. 73–79.
[28] A. Toselli, Some results on overlapping Schwarz methods for the Helmholtz equation employing perfectly matched layers, Technical Report 765, Courant Institute, 1998.
[29] L. Zschiedrich, S. Burger, R. Klose, A. Schädle, F. Schmidt, JCMmode: An adaptive finite element solver for the computation of leaky modes, in: Y. Sidorin, C.A. Wächter (Eds.), Integrated Optics: Devices, Materials, and Technologies IX, vol. 5728, SPIE, Bellingham, Washington, USA, 2005, pp. 192–202.
[30] L. Zschiedrich, S. Burger, A. Schädle, F. Schmidt, Domain decomposition method for electromagnetic scattering problems, in: Proceedings of the 5th International Conference on Numerical Simulation of Optoelectronic Devices, IEEE, ISBN: 0-7803-9149-7. 2005, pp. 55–56.
[31] Lin Zschiedrich, Sven Burger, Benjamin Kettner, Frank Schmidt, Advanced finite element method for nano-resonators, in: M. Osinski et al. (Eds.), Physics and Simulation of Optoelectronic Devices XIV, vol. 6115, SPIE, Bellingham, Washington, USA, 2006, pp. 164–174.